**Naval Research Laboratory**
Washington, DC 20375-5320



NRL/MR/6790--94-7465

# Propagation of Radius-Tailored Laser Pulses Over Extended Distances in a Uniform Plasma

J. KRALL
E. ESAREY
P. SPRANGLE
G. JOYCE

*Beam Physics Branch*
*Plasma Physics Division*



May 18, 1994



Approved for public release; distribution unlimited.

# REPORT DOCUMENTATION PAGE

*Form Approved*
*OMB No. 0704-0188*



| 1. AGENCY USE ONLY (*Leave Blank*) | 2. REPORT DATE | 3. REPORT TYPE AND DATES COVERED |
|---|---|---|
| | May 18, 1994 | Interim |

**4. TITLE AND SUBTITLE**

Propagation of Radius-Tailored Laser Pulses Over Extended Distances in a Uniform Plasma

**5. FUNDING NUMBERS**

DOE-AI05-83ER40117
JO -67-0899-04

**6. AUTHOR(S)**

J. Krall, E. Esarey, P. Sprangle and G. Joyce

**7. PERFORMING ORGANIZATION NAME(S) AND ADDRESS(ES)**

Naval Research Laboratory
Washington, DC 20375-5320

**8. PERFORMING ORGANIZATION REPORT NUMBER**

NRL/MR/6790--94-7465

**9. SPONSORING/MONITORING AGENCY NAME(S) AND ADDRESS(ES)**

Office of Naval Research
800 North Quincy Street
Arlington, VA 22217-5660

Department of Energy
Arlington, VA 22217

**10. SPONSORING/MONITORING AGENCY REPORT NUMBER**

**11. SUPPLEMENTARY NOTES**

**12a. DISTRIBUTION/AVAILABILITY STATEMENT**

Approved for public release; distribution unlimited.

**12b. DISTRIBUTION CODE**

**13. ABSTRACT** (*Maximum 200 words*)

A Maxwell-fluid model is described, which allows simulation of laser pulses over extended distances (multiple diffraction lengths) in an underdense plasma. This model is used to simulate radius-tailored laser pulses, which can propagate over such distances with minimal distortion in a uniform plasma. Theoretical model equations governing the choice of radius tailoring are also given. A radius-tailored pulse has constant power approximately equal to the critical power for relativistic guiding over the length of the pulse and a spot size at focus that varies over the length of the pulse. A laser pulse configuration of this type can be constructed from a series of ultra-short Gaussian pulses.

**14. SUBJECT TERMS**

Laser-plasma
Particle acceleration

**15. NUMBER OF PAGES**

26

**16. PRICE CODE**

| 17. SECURITY CLASSIFICATION OF REPORT | 18. SECURITY CLASSIFICATION OF THIS PAGE | 19. SECURITY CLASSIFICATION OF ABSTRACT | 20. LIMITATION OF ABSTRACT |
|---|---|---|---|
| UNCLASSIFIED | UNCLASSIFIED | UNCLASSIFIED | UL |

NSN 7540-01-280-5500

Standard Form 298 (Rev. 2-89)
Prescribed by ANSI Std 239-18
298-102

CONTENTS

# Propagation of Radius–Tailored Laser Pulses Over Extended Distances in a Uniform Plasma

## I. Introduction

The physics of intense laser pulse propagation in an underdense plasma is a problem of recent interest for a variety of applications,[1,2] including radiation generation (laser harmonics, x-ray sources) and advanced accelerators (laser wake-field accelerator, plasma beat-wave accelerator). Some applications, particularly the laser wake-field accelerator (LWFA), require laser propagation over several laser diffraction lengths at ultra-high laser intensities. In the LWFA,[3-8] a short ($\tau_L < 1$ ps), high power ($P > 1$ TW) laser pulse propagates in plasma to generate a large amplitude ($E_z > 1$ GV/m) wake field, which can trap and accelerate a trailing electron bunch.

Ultra-high-intensity laser pulses require a tight focus and are characterized by an intensity high enough that relativistic effects become significant ($a_0 \simeq 1$) and a vacuum diffraction length, or Rayleigh length $Z_R$, that is is relatively short ($Z_R < 1$ cm). Here, $a_0 = eA_0/m_ec^2$ is the peak amplitude of the normalized vector potential of the laser pulse, $Z_R = \pi r_0^2/\lambda$, $r_0$ is the laser spot size at focus, $\lambda$ is the laser wavelength, $m_e$ is the electron mass, and a Gaussian radial profile has been assumed. In terms of the peak laser intensity $I$, $a_0 \simeq 8.5 \times 10^{-10}\lambda[\mu\text{m}]I^{1/2}[\text{W/cm}^2]$ for linear polarization, which will be assumed throughout this paper.

Computer simulations of such laser pulses can be problematical because of the disparate time and length scales involved. Typically, $\lambda \ll L \ll Z_R$, where the laser pulse length $L = c\tau_L$ is defined as the full-width-at-half-maximum of the laser intensity. A numerical code, LEM (Laser-ElectroMagnetic), has been developed to simulate laser propagation in an underdense plasma for arbitrarily high values of $a_0$. It is based on the cold-fluid model equations given in Refs. 7 and 8. In developing this code, the model equations for the plasma response to a given laser field were recast in a numerically tractable form. In this paper, the numerical equations are presented and, as an example, the code is applied to the propagation of radius–tailored laser pulses. Theoretical model equations governing the choice of radius tailoring are also given.

Manuscript approved March 16, 1994.

Radius–tailored laser pulses, which were discussed briefly in Ref. 7, have a unique property in that they can propagate over extended distances ($> 10Z_R$) in a uniform underdense plasma. While previous simulations of such pulses[7] were performed in the context of the paraxial approximation, which gives a constant laser group velocity $v_g = c$, the present study shows that, for cases of interest, variations in the group velocity of the laser pulse over the length of the pulse can have a significant effect. In the present study, theoretical model equations governing the choice of the axial pulse profile for radius tailoring are discussed and parameter requirements and tolerances are given for such pulses and for the injection of these pulses into a plasma. Also, the construction of a radius–tailored laser pulse from from a series ultra-short Gaussian pulses is considered.

## II. Model Equations

These simulations were based on the laser-plasma fluid model described in Refs. 7 and 8, which utilizes $(r, \zeta = z - ct, \tau = t)$ coordinates. The laser pulse moves in the positive $z$ direction such that the front of the laser pulse remains near $\zeta = 0$. The physical region of interest extends from $\zeta = 0$, where the plasma is unperturbed, to $\zeta < 0$. The model, which takes advantage of the separation between the fast $(\lambda)$ and slow $(Z_R, \lambda_p)$ time and space scales, is valid when $Z_R \gg L$, $Z_R \gg \lambda_p$, $\lambda \ll r_0$, and $\lambda \ll \lambda_p$, where $\lambda_p = 2\pi c/\omega_p$ is the plasma wavelength, $\omega_p = (4\pi e^2 n_0/m_e)^{1/2}$ is the electron plasma frequency, $n_0 = n^{(0)}(r = 0)$ and $n^{(0)}(r)$ is the initial electron density profile (in the simulations shown below, an initially uniform plasma radial density profile is assumed). Laser pulse evolution is described by the wave equation

$$\left(\nabla_\perp^2 + \frac{2ik}{c}\frac{\partial}{\partial\tau} + \frac{2}{c}\frac{\partial^2}{\partial\zeta\partial\tau}\right)\hat{\mathbf{a}}_f = k_p^2\rho_s\hat{\mathbf{a}}_f. \tag{1}$$

To include variations in the laser group velocity, the $\partial^2/\partial\zeta\partial\tau$ term is retained in Eq. (1), in contrast to Ref. 7. In Eq. (1), $\mathbf{a}_f = e\mathbf{A}_f/m_e c^2$ is normalised vector potential of the laser pulse, $\hat{\mathbf{a}}_f$ is the slowly varying amplitude ($\mathbf{a}_f = \hat{\mathbf{a}}_f \exp(ik_0\zeta)/2 + c.c$, where $c.c.$ denotes complex conjugate), $k_p = \omega_p/c$, $\rho_s = n_s/\gamma_s n_0$, $n_s$ is the plasma density, $\gamma_s$ is the relativistic factor of the plasma, and the subscript $s$ denotes a slowly-varying component. The plasma response to a given laser field $\hat{\mathbf{a}}_f$ is given by[7,8]

$$\nabla_\perp^2\mathbf{a}_s = k_p^2\rho_s\mathbf{u}_s - \frac{\partial}{\partial\zeta}\nabla\phi_s, \tag{2a}$$

$$\left(\nabla_\perp^2 + \frac{\partial^2}{\partial\zeta^2}\right)\phi_s = k_p^2\left(\gamma_s\rho_s - \rho^{(0)}\right), \tag{2b}$$

$$\frac{\partial}{\partial\zeta}(\mathbf{u}_s - \mathbf{a}_s) = \nabla(\gamma_s - \phi_s), \tag{2c}$$

and

$$\gamma_s = 1 + \frac{u_{\perp,s}^2 + |\hat{\mathbf{a}}_f|^2/2 + \psi_s^2}{2(1+\psi_s)}. \tag{2d}$$

where the Coulomb gauge has been used ($\nabla\cdot\mathbf{a}_s = 0$) and $\psi_s = \phi_s - a_{z,s}$. In Eqs. (2a-d), $\mathbf{a}_s = e\mathbf{A}_s/mc^2$ and $\phi_s = e\Phi_s/mc^2$ are the normalised vector and scalar potentials,

respectively, $\mathbf{u}_s = \mathbf{p}_s/mc$ is the normalized momentum, $\rho^{(0)} = \rho_s(\zeta = 0)$, and the plasma ions are assumed to be immobile.

In the axisymmetric case, Eqs. (2a-d), along with $\nabla \cdot \mathbf{a}_s = 0$, can be combined to yield a single equation[7,8] of the form $\partial^2\psi_s/\partial\zeta^2 = G(\psi_s, |\hat{\mathbf{a}}_f|^2)$. This equation can be written as

$$\frac{\partial^2\psi_s}{\partial\zeta^2} = \left(k_p^2\rho_s - \nabla_\perp^2\right) u_{z,s} + \frac{\partial}{\partial\zeta}\left(\nabla_\perp \cdot \mathbf{u}_{\perp,s}\right), \tag{3a}$$

where $u_{z,s} = \gamma_s - \psi_s - 1$,

$$\mathbf{u}_{\perp,s} = \frac{1}{k_p^2\rho_s}\frac{\partial}{\partial\zeta}(\nabla_\perp\psi_s), \tag{3b}$$

and

$$\rho_s = \frac{1}{(1+\psi_s)}\left(\rho^{(0)} + k_p^{-2}\nabla_\perp^2\psi_s\right). \tag{3c}$$

A form of equation (3a) is solved numerically to obtain the plasma response. Both the derivation of Eqs. (3a-c) and the details of the numerical solution are discussed in the Appendix.

The LEM code has been used to simulate the effects of several instabilities of recent interest, such as the forward Raman scattering (FRS) instability[8] and the self-modulation instability.[6,8,9] Certain instabilities, however, cannot be adequately described using the formulation given here. In particular, the growth large-angle Raman scattering, also called Raman side-scatter (RSS),[10,11] is suppressed by the numerical scheme, which includes a radial smoothing algorithm. This smoothing algorithm is required to suppress a numerical instability and is discussed in the Appendix.

It is reasonable to neglect the effect of RSS on the simulation results given below because of the short pulse duration ($k_pL \simeq 12$) and because the intensity varies over the length of the pulse. Specifically, Ref. 10 indicates that the growth of RSS over the length of the pulse is minimal for short pulses with $k_pL < 10 - 20$. Furthermore, additional simulations of radius–tailored pulses, with $k_pL \gg 10$, showed that the growth of the FRS and self-modulation instabilities were strongly suppressed by the radius tailoring. This suggests that radius tailoring may also suppress large-angle Raman scattering.

## III. Radius–Tailored Laser Pulses

A radius–tailored laser pulse is a pulse configuration which is designed to to propagate over a long distance by the mechanism of relativistic optical guiding.[12,13] Relativistic optical guiding, which generally occurs when the laser power $P_0 \simeq 21.5(a_0 r_0/\lambda)^2$ GW exceeds the critical power $P_c \simeq 17(\lambda_p/\lambda)^2$ GW, where $P_0/P_c = (k_p r_0 a_0)^2/32$, is problematical because the leading portion of a laser pulse ($|\zeta| < \lambda_p$) tends to diffract as if in vacuum[5,7] and because long pulses ($L > \lambda_p$) tend to undergo self-modulation.[6-10] With radius tailoring, the laser spot size at focus is tapered from a large value at the pulse front to a small value over the length of the laser pulse while keeping $P/P_c \simeq 1$ throughout the pulse. This condition is met when $a_L(\zeta) r_L(\zeta) \simeq 0.9\lambda_p$, where $r_L$ is the laser spot size and $a_L = |\hat{a}_f|$. Radius tailoring is designed to relativistically guide the high intensity portion of the laser pulse while allowing the leading portion of the pulse to simply diffract. The tapered radius produces a locally large diffraction length at the pulse front, $Z_{R,0}(\zeta = 0) \gg Z_{R,0}(\zeta = -L)$, where $Z_{R,0} = \pi r_L(\zeta, \tau = 0)/\lambda$. Hence, the pulse can remain focused over large distances $c\tau \gg Z_{R,0}(\zeta = -L)$. Furthermore, self-modulation is suppressed for $L \lesssim 2\lambda_p$ because the increasing laser intensity over the length of the pulse does not excite a strong wake field within the pulse. Note that while the spot size at focus varies along the length of the pulse, each point along the pulse must reach its focus simultaneously.

The selection of a pulse profile is motivated by considering the envelope equation of Ref. 9, which describes the evolution of the laser spot size $r_L(\zeta, \tau)$ of a pulse with an approximately Gaussian radial profile in the limits $a^2 \ll 1$, $r_L^2 k_p^2 \gg 1$. Assuming an initially uniform plasma, the envelope equation can be written as

$$\frac{\partial^2 R}{\partial \tau^2} - \frac{c^2}{Z_R^2 R^3}\left\{1 - 4R^4 k_p \int_\zeta^0 d\zeta' \sin[k_p(\zeta' - \zeta)] \frac{P(\zeta')/P_c}{[R^2(\zeta) + R^2(\zeta')]^2}\right\} = 0, \qquad (4)$$

where $R = r_L(\zeta, \tau)/r_0$, $r_0$ is now defined to be a constant equal to the minimum spot size at focus (corresponding to the peak value of $|\hat{a}_f| = a_0$) and $Z_R = \pi r_0^2/\lambda$. The second term in Eq. (4) represents vacuum diffraction whereas the third term represents the focusing/diffractive effects of the plasma.

Initially, for $c\tau \ll |Z_{R,eff}|$, $R \simeq R(\tau = 0)[1 + (c\tau/Z_{R,eff})^2]^{1/2}$, where the inverse of

the effective diffraction length $\kappa^2 = 1/Z_{R,eff}^2$ is

$$\kappa^2 = \frac{1}{Z_{R,0}^2(\zeta)} \left\{ 1 - 4R^4 k_p \int_\zeta^0 d\zeta' \sin[k_p(\zeta' - \zeta)] \frac{P(\zeta')/P_c}{[R^2(\zeta) + R^2(\zeta')]^2} \right\}. \quad (5)$$

In this notation, $\kappa = 1/Z_{R,0}$ corresponds to vacuum diffraction, $\kappa = 0$ indicates a "matched" $\zeta$-slice (focusing and diffraction forces are balanced) and $\kappa^2 < 0$ corresponds to net focusing. The choice of initial pulse profile, specified as $P(\zeta)$ and $a_L(\zeta, \tau = 0)$, is motivated by the desire to have $\kappa$ vary smoothly from $\kappa = 1/Z_{R,0}(\zeta = 0)$ at the leading edge of the pulse to $\kappa \simeq 0$ at the tail of the pulse.

To illustrate, consider four radius-tailored pulse configurations, each at constant power: (a) $a_L = a_0 \sin(-\zeta\pi/4\lambda_p)$, $0 \le -\zeta \le 2\lambda_p$, $P = P_c$; (b) Case (a) with $P = 1.2P_c$; (c) $a_L^2 = -\zeta a_0^2/2\lambda_p$, $0 \le -\zeta \le 2\lambda_p$, $P = P_c$; (d) Case (c) with $P = 1.14P_c$. Plots of $(\kappa Z_R)^2$ versus $\zeta$ are shown for each case in Fig. 1. Here, $(\kappa Z_R)^2 = Z_R^2/Z_{R,eff}^2(\zeta)$ is a measure of the initial rates of diffraction/focusing throughout the pulse relative to the vacuum diffraction rate associated with the back of the pulse. For comparison $(\kappa Z_R)^2$ for a rectangular pulse with $a_L = a_0$, $0 \le -\zeta \le 2\lambda_p$, and $P = P_c$, is shown in Fig. 2. Figures 1 and 2 illustrate key phenomena that have been observed in LEM simulations of tailored and non-tailored laser pulses.

The most significant diffraction in Fig. 1 is observed at the peak of $(\kappa Z_R)^2$ near the beam head ($|\zeta| < \lambda_p/2$), where the laser is everywhere slowly diffracting. For example, the peak diffraction in case (a) occurs at $\zeta \simeq -0.65\lambda_p$, where $(\kappa Z_R)^2 = 0.015$. This corresponds to $Z_{R,eff} = 8.2Z_R$. The peak diffraction near the beam head can be reduced by increasing the laser power in this region. In case (b), the peak diffraction corresponds to $Z_{R,eff} = 10.5Z_R$. This suggests that a carefully designed tailored pulse might have peak power somewhat greater than $P_c$ at and near the pulse head, tapering to $P \simeq P_c$ at the tail of the pulse.

For constant $P/P_c$, there is a trade-off between diffraction near the head and over-focusing in the body of the pulse. Simulations show that, at $r_0 = \lambda_p$, the allowable range is $1 \le P/P_c \le 1.5$, with optimum results at $P/P_c \simeq 1.2$. While a detailed study has not been performed, it is clear that this tolerance will vary with $r_0$. In particular, for $r_0 \gg \lambda_p$ and $P > P_c$, simulations have verified that the relativistically-focused tail portion of the

pulse is far from radial equilibrium. For $P > P_c$, a laser pulse in a transverse equilibrium state[12,13] has a characteristic radius $r_{eq} < \lambda_p$.

The tendency of non–tailored laser pulses to erode[5,7] is illustrated in Fig. 2, which indicates diffraction over a region of length $\lambda_p/4$ near the head of the rectangular pulse ($Z_{R,eff} = Z_R$ at the pulse head). Figure 2 also shows regions of focusing and defocusing which lead to the self-modulation instability of Refs. 6-10. These periodic regions are due to the plasma wave generated by the rise time $L_{rise}/c$ of the pulse (for a square pulse, $k_p^2 L_{rise}^2 \ll 1$). Figure 1 shows that radius–tailored pulses also have this tendency, but to a lesser degree (the characteristic defocusing lengths are smaller by approximately an order of magnitude). Simulations show that for $L \gg \lambda_p$ self-modulation can be a significant effect, even for radius-tailored laser pulses.

## IV. Simulations

As an example of radius–tailored laser pulse propagation, consider a laser pulse with radius tailoring over the region $0 \leq -\zeta \leq 2\lambda_p$, where $P = 1.14P_c$ and $a_L^2 = -\zeta a_0^2/2\lambda_p$ as in case (c) above, and decreasing power over the region $2\lambda_p < -\zeta \leq 5\lambda_p/2$, where $r_L = r_0$ and $a_L^2 = -2a_0^2(\zeta + 2\lambda_p)/\lambda_p$. With $a_0 = 0.96$ and plasma density $n_0 = 5.5 \times 10^{17}$ cm$^{-3}$, we have $r_0 = \lambda_p = 45$ $\mu$m, $P_c = 35$TW, $P_0 = 40$TW, and $Z_R = 45\pi\lambda_p = 0.64$cm.

The simulation begins at $\tau = 0$ with the laser pulse outside the plasma, one $Z_R$ away from the focal point. The transition from vacuum to full plasma density occurs over a distance of $0.3Z_R$ such that full density is reached at the focal point. Simulations show that with a longer transition region, the laser over-focuses and the effectiveness of radius tailoring is reduced. The simulation continues until $c\tau = 16Z_R$.

Figure 3 shows plots of the normalized laser intensity $|\hat{a}_f|^2$ at $c\tau = Z_R$, as the pulse enters the plasma with a minimum spot size $r_{L,min} = \lambda_p$, and at $c\tau = 16Z_R$, where the minimum spot size is $r_{L,min} = 0.59\lambda_p$. In this code, the $r_L$ is the radius enclosing 86.5% of the laser power (for a Gaussian pulse, $a \sim e^{-r^2/r_L^2}$).

Several interesting effects have been observed in this and in other LEM simulations. Firstly, the laser pulse deviates from its initial Gaussian profile, becoming highly peaked on axis. As a result, the quantity $a_L r_L$ does not remain constant. Secondly, because $v_g < c$, there is a noticeable degree of slippage in the $\zeta$-position of the pulse versus time. Thirdly, because of nonlinear effects, $v_g$ varies with the laser intensity.[5,14] The tendency of the laser to "steepen" and develop a peaked profile versus $\zeta$ can be attributed to this effect. In fact, the range of validity of these simulations was limited by this tendency: when $a_L|\partial a_L/\partial\zeta|^{-1} \simeq \lambda$, Eqs. (2a)-(2d) no longer hold. Fourthly, a large amplitude wake field, with $E_z \simeq 30$ GV/m, is generated behind the laser pulse.

Note that the results stated above and in the previous section indicate requirements on plasma uniformity and on the sharpness of the vacuum-plasma boundary. Because $P_c \sim 1/n_0$, the requirement that $1 \leq P/P_c \leq 1.5$ indicates that a variation in $n_0$ as large as $\pm 15\%$ is acceptable for a radius-tailored pulse with uniform power. This was verified to some degree in simulations of radius-tailored pulses in which the plasma density varied by $\pm 10\%$ with 2–4 oscillations per $Z_R$. These density variations produced no discernible

change in the results. When the laser power is nonuniform, as in the cases below, this requirement becomes somewhat more strict. The requirement, stated above, that the vacuum-plasma interface have a width smaller than $0.3Z_R$ should not pose a significant difficulty, since $Z_R \gg \lambda_p$ for typical tailored-pulse parameters.

While the ideal laser pulse configuration of Fig. 3 may be difficult to produce in the laboratory, it may be possible to construct an approximate radius-tailored pulse through the superposition of several ultra-short pulses, each with a different spot size. A somewhat idealized configuration of 5 overlapping laser pulses is shown in Fig. 4. Each pulse has a Gaussian radial profile and an axial profile given by $a_L \sim \sin(-\zeta\pi/2L), 0 \leq -\zeta \leq 2L$, with $L = 17$ $\mu$m (L/c = 57 fs). This configuration is idealized in the sense that the overlapping pulses are phase-locked, resulting in constructive interference, and the separation between pulses is 23 $\mu$m such that the variation in power along the pulse is minimized with peak power $P_{peak} \simeq P_0 = 40$ TW, as in Fig. 3, and $\zeta$-averaged power $\langle P \rangle \simeq P_c$. This simulation is otherwise identical to that shown in Fig. 3. As in that case, a large amplitude wake field $E_z \simeq 25$ GV/m is generated behind the laser pulse.

A less ideal configuration of overlapping short pulses is illustrated in Fig. 5. Here, the idealization of phase-locking is removed, with each pulse having a randomly-chosen phase shift. Since tailored pulse simulations at $r_0 = \lambda_p$ show successful guiding for $1 \leq P/P_c \leq 1.5$, the pulse spacing has been decreased to 20 $\mu$m. Thus, in the case of perfect constructive interference, $P_{peak} \simeq 1.5P_0$, where again $P_0 = 40$ TW. Because this configuration contains a random phase-shift for each pulse, the results from an ensemble of simulations must be considered. For practical reasons, a statistically small ensemble of 20 simulations was used. Of these, five were deemed "successful", i.e., a wake with $E_z \geq 20$ GV/m persisted over a propagation range greater than 10 $Z_R$. Results from one such case are given in Figs. 5 and 6, with Fig. 5 showing the laser intensity plotted at $c\tau = Z_R$ and at $c\tau = 11Z_R$, and Fig. 6 showing the laser power plotted versus $\zeta$ at $\tau = 0$. For comparison, $P$ versus $\zeta$ is also shown for the ideal phase-locked case of Fig. 3. The results of the remaining 15 simulations were characterized by the axial break-up of the laser pulse. In many of these cases, one or more of the resulting "beamlets" propagated greater than 10 $Z_R$, but with a reduced wake amplitude ($E_z \leq 15$ GV/m).

Clearly, experimental confirmation of the results of Figs. 4 and 5 would be difficult. While it is beyond the scope of this paper to provide an experimental design, it seems reasonable to speculate that in such an experiment a long laser pulse would be split into five separate pulses with separate optical paths. The optics would have to be tuned in such a way that the pulses arrive at focus simultaneously. Only small errors in the relative timing and focal positions ($\ll 20\ \mu$m) would be allowed. It is not clear whether or not such an experiment could be performed using present technology.

## V. Conclusions

The numerical fluid code LEM, described above and in the Appendix, allows simulation of intense laser pulses over extended distances ($c\tau \gg Z_R$). Because the code computes the evolution of the laser envelope on the plasma time-scale, these simulations are significantly faster than those carried out by more conventional means, such as the particle-in-cell method. Simulations of radius–tailored laser pulses propagating in a uniform underdense plasma show that such pulses can remain focused over distances greater than $10Z_R$ in accordance with Eq. (5), which was derived from the laser-plasma envelope equation of Ref. 9. These simulations show that large amplitude wake fields ($E_z > 1$ GV/m) can be generated behind the radius-tailored pulse provided that the intensity terminates in less than a plasma wavelength. Simulations also show that a radius–tailored laser pulse can be constructed from a series of overlapping ultra-short ($L/c \sim 50fs$) Gaussian pulses.

## Acknowledgements

The authors would like to thank A. Ting (Naval Research Laboratory) for numerous enlightening discussions. This work was supported by the Department of Energy and the Office of Naval Research.

## Appendix: Numerical Solution of the Model Equations

The model equations are given as Eqs. (2a-d) in the main text. These equations make use of the quasi-static approximation, in which it is assumed that the scale length over which the laser field evolves is long compared to the laser pulse length ($Z_R \gg L$). In this limit derivatives with respect to $\tau$ are dropped relative to derivatives with respect to $\zeta$ in the plasma fluid equations, but not in the wave equation. In addition, Eqs. (1) and (2a-d) have been averaged over the fast ($\lambda$) laser oscillations. The resulting simulation code, LEM (Laser-ElectroMagnetic), describes the laser envelope $\hat{a}_f$ and the plasma response on a spatial grid that resolves $\lambda_p, L$ and $r_0$, with a time step that resolves the evolution of the laser intensity ($Z_R/c$) and the phase oscillations, due to plasma dispersion, of the real and imaginary parts of $\hat{a}_f$, which have a characteristic period $k\lambda_p^2/\pi c$.

Equations (2a-d) are numerically intractable in the sense that it is not clear which equation should be solved first, second, etc., or if an iterative method of solving the equations can be expected to converge to a meaningful solution. This numerical quagmire can be avoided by recasting the problem into a single equation for the quantity $\psi_s$, given as Eq. (3a) in the main text. An outline of the derivation of Eqs. (3a-c) is as follows. The axial component of Eq. (2c) yields the constant of motion $u_{z,s} = \gamma_s - \psi_s - 1$. Substituting $\phi_s = \psi_s + a_{z,s}$ into the axial component of Eq. (2a) gives

$$\frac{\partial^2 \psi_s}{\partial \zeta^2} = k_p^2 \rho_s u_{z,s} - \nabla^2 a_{z,s}. \qquad (A1)$$

Subtracting this from Poisson's equation, Eq. (2b), gives Eq. (3c) for $\rho_s$ in terms of $\psi_s$. Assuming axisymmetry ($\partial/\partial\theta = 0$), Eqs. (2c) and (2a) imply $u_{\theta,s} = a_{\theta,s} = 0$. Substituting $\phi_s = \psi_s + a_{z,s}$ into the transverse component of Eq. (2a) and using $\nabla \cdot \mathbf{a}_s = 0$ and $u_{\theta,s} = a_{\theta,s} = 0$ gives Eq. (3b) for $\mathbf{u}_{\perp,s}$ in terms of $\psi_s$. Operating on Eq. (2c) with $(\nabla_\perp \cdot)$ and using the gauge condition and the constant of motion gives

$$\nabla^2 a_{z,s} = \nabla_\perp^2 u_{z,s} - \frac{\partial}{\partial \zeta}(\nabla_\perp \cdot \mathbf{u}_{\perp,s}). \qquad (A2)$$

Equation (3a) for $\partial^2 \psi_s / \partial \zeta^2$ results from substituting Eq. (A2) into Eq. (A1).

Equation (3a) can be written in the following form:

$$\left[1-\frac{\nabla_\perp^2}{k_p^2\rho_s}+\left(\frac{\nabla_\perp\rho_s}{k_p^2\rho_s^2}\right)\cdot\nabla_\perp\right]\frac{\partial^2\psi_s}{\partial\zeta^2}$$
$$=\left[1-\frac{\nabla_\perp^2}{k_p^2\rho_s}+\left(\frac{\nabla_\perp\rho_s}{k_p^2\rho_s^2}\right)\cdot\nabla_\perp\right]k_p^2\rho_s u_{z,s} \qquad (A3)$$
$$+\nabla_\perp\cdot\left[k_p^{-2}\left(\frac{\partial\rho_s^{-1}}{\partial\zeta}\right)\nabla_\perp\frac{\partial\psi_s}{\partial\zeta}+\frac{u_{z,s}}{\rho_s}\nabla_\perp\rho_s\right].$$

The quantities $\rho_s$ and $u_{z,s}$ can be written as functions of $\psi_s$ and $|\hat{a}_f|^2$ using $u_{z,s}=\gamma_s-\psi_s-1$ along with Eqs. (2d), (3b) and (3c). Equation (A3) can be integrated numerically in $\zeta$ in a straightforward manner by starting at the $\zeta=0$ boundary, where the plasma is unperturbed and where $\psi_s=\nabla_\perp\psi_s=\nabla_\perp^2\psi_s=\partial\psi_s/\partial\zeta=0$ is assumed. For the purposes of numerical solution, the form of Eq. (A3) is preferable to that of Eq. (3a) because the second-order derivative $\partial^2\psi_s/\partial\zeta^2$, which occurs in the last term on the right side of Eq. (3a), now appears on the left side of Eq. (A3). Radial boundary conditions in Eq. (A3) are dictated by axisymmetry at $r=0$ and by the imposition of a metallic wall at $r=r_w\gg r_0$. Equations (1) and (A3), along with the auxiliary Eqs. (2d), (3c) and (3d), provide a complete description of the laser-plasma interaction on the plasma time scale.

In numerically integrating Eq. (A3) versus $\zeta$, care must be taken to avoid a numerical instability wherein a sufficiently large disturbance in $\psi_s$ with a sufficiently large transverse wavenumber grows exponentially as a function of $\zeta$. This can be seen heuristically by considering a small amplitude electrostatic wake field in a uniform plasma ($\rho^{(0)}=1$) with $\gamma_s-1<\psi_s<1$ and $a_{z,s}\simeq 0$. In this case, Eq. (A1) can be written

$$\frac{\partial^2\psi_s}{\partial\zeta^2}=-(k_p^2+k_\perp^2\hat{\psi}_s)\psi_s, \qquad (A4)$$

where $\psi_s(\zeta,x)=\hat{\psi}_s(\zeta,k_\perp)e^{-ik_\perp x}$ and $x$ is the transverse coordinate. For $k_\perp^2\hat{\psi}_s\ll k_p^2$, Eq. (A4) produces the usual oscillatory wake field, with wavenumber $k_p$. However, a numerical instability occurs for any transverse wavenumber that satisfies $k_\perp^2>k_p^2/\hat{\psi}_s(k_\perp)$. In particular, consider the Nyquist wavenumber $k_N=\pi/\Delta x$ (the highest wavenumber that can be carried on the numerical grid), where $\Delta x$ is the transverse grid spacing. The stability requirement is that any numerical "noise" at $k=k_N$ must be have a very small

amplitude: $\hat{\psi}_s(k_N) < (2\Delta x/\lambda_p)^2$. From Eq. (3c) it can be shown the instability condition $k_\perp^2 > k_p^2/\hat{\psi}_s(k_\perp)$ corresponds to a negative plasma electron density, an unphysical situation. The instability is therefore numerical in nature and is avoided by filtering out the high transverse wavenumbers ($k_\perp \gg 1/r_0$) from $\psi_s$.

## References


1. G. Mourou and D. Umstadter, Phys. Fluids B 4, 2315 (1992); J. P. Watteau, G. Bonnaud, J. Coutant, R. Dautray, A. Decoster, M. Louis-Jacquet, J. Ouvry, J. Sauteret, S. Seznec, D. Teychenne, Phys. Fluids B 4, 2217 (1992); P. Sprangle and E. Esarey, Phys. Fluids B 4, 2241 (1992).
2. *Advanced Accelerator Concepts*, Edited by J. S. Wurtele, AIP Conference Proceedings **279** (American Institute of Physics, New York, 1993).
3. T. Tajima and J. M. Dawson, Phys. Rev. Lett. **43**, 267 (1979); L. M. Gorbunov and V. I. Kirsanov, Sov. Phys. JETP **66**, 290 (1987); V. N. Tsytovich, U. DeAngelis and R. Bingham, Comments Plasma Phys. Controlled Fusion **12**, 249 (1989); V. I. Bereshiani and I. G. Murusidze, Phys. Lett. A **148**, 338 (1990).
4. P. Sprangle, E. Esarey, A. Ting and G. Joyce, Appl. Phys. Lett. **53**, 2146 (1988); E. Esarey, A. Ting, P. Sprangle and G. Joyce, Comments Plasma Phys. Controlled Fusion **12**, 191 (1989).
5. P. Sprangle, E. Esarey and A. Ting, Phys. Rev. Lett. **64**, 2011 (1990); Phys. Rev. A **41**, 4463 (1990); A. Ting, E. Esarey and P. Sprangle, Phys. Fluids B **2**, 1390 (1990).
6. N. E. Andreev, L. M. Gorbunov, V. I. Kirsanov, A. A. Pogosova and R. R. Ramazashvili, Pis'ma Zh. Eksp. Teor. Fiz. **55**, 551 (1992).
7. P. Sprangle, E. Esarey, J. Krall and G. Joyce, Phys. Rev. Lett. **69**, 2200 (1992); E. Esarey, P. Sprangle, J. Krall, A. Ting and G. Joyce, Phys. Fluids B **5**, 2690 (1993).
8. J. Krall, A. Ting, E. Esarey and P. Sprangle, Phys. Rev. E **48**, 2157 (1993).
9. E. Esarey, J. Krall and P. Sprangle, "Envelope Analysis of Laser Self-Focusing and Self-Modulation in a Plasma", submitted to Phys. Rev. Lett.
10. T. M. Antonsen, Jr. and P. Mora, Phys. Rev. Lett. **69**, 2204 (1992); Phys. Fluids B **5**, 1440 (1993).
11. C. B. Darrow, C. Coverdale, M. D. Perry, W. B. Mori, C. Clayton, K. Marsh and C. Joshi, Phys. Rev. Lett. **69**, 442 (1992); W. P. Leemans, C. E. Clayton, W. B. Mori, K. A. Marsh, P. K. Kaw, A. Dyson, C. Joshi and J. M. Wallace, Phys. Rev. A **46**, 1091 (1992).

12. A. G. Litvak, Zh. Eksp. Teor. Fiz. **57**, 629 (1969) [Sov. Phys. JETP **30**, 344 (1969)]; C.E. Max, J. Arons and A.B. Langdon, Phys. Rev. Lett. **33**, 209 (1974); G. Schmidt and W. Horton, Comments Plasma Phys. Controlled Fusion **9**, 85 (1985); P. Sprangle, C.M. Tang and E. Esarey, IEEE Trans. Plasma Sci. **PS-15**, 145 (1987); E. Esarey, A. Ting and P. Sprangle, Appl. Phys. Lett. **53**, 1266 (1988); W.B. Mori, C. Joshi, J.M. Dawson, D.W. Forslund and I.M. Kindel, Phys. Rev. Lett. **60**, 1298 (1988); P. Gibbon and A.R. Bell, Phys. Rev. Lett. **61**, 1599 (1988); C.J. McKinstrie and D.A. Russell, Phys. Rev. Lett. **61**, 2929 (1988).

13. G.Z. Sun, E. Ott, Y.C. Lee and P. Guzdar, Phys. Fluids **30**, 526 (1987); T. Kurki-Suonio, P.J. Morrison and T. Tajima, Phys. Rev. A **40**, 3230 (1989); P. Sprangle, A. Zigler and E. Esarey, Appl. Phys. Lett. **58**, 346 (1991); A.B. Borisov, A.V. Borovskiy, O.B. Shiryaev, V.V. Korobkin, A.M. Prokhorov, J.C. Solem, T.S. Luk, K. Boyer and C. K. Rhodes, Phys. Rev. A **45**, 5830 (1992). L.A. Abramyan, A.G. Litvak, V.A. Mironv and A.M. Sergeev, Zh. Eksp. Teor. Fiz. **102**, 1816 (1992) [Sov. Phys. JETP **75**, 978 (1992)]; X.L. Chen and R.N. Sudan, Phys. Fluids B **5**, 1336 (1993); H.S. Brandi, C. Manus, G. Mainfray, T. Lehner and G. Bonnaud, Phys. Fluids B **5**, 3539 (1993).

14. H. H. Kuehl, C. Y. Zhang and T. Katsouleas, Phys. Rev. E **47**, 1249 (1993); C. D. Decker and W. B. Mori (private communication, 1992).

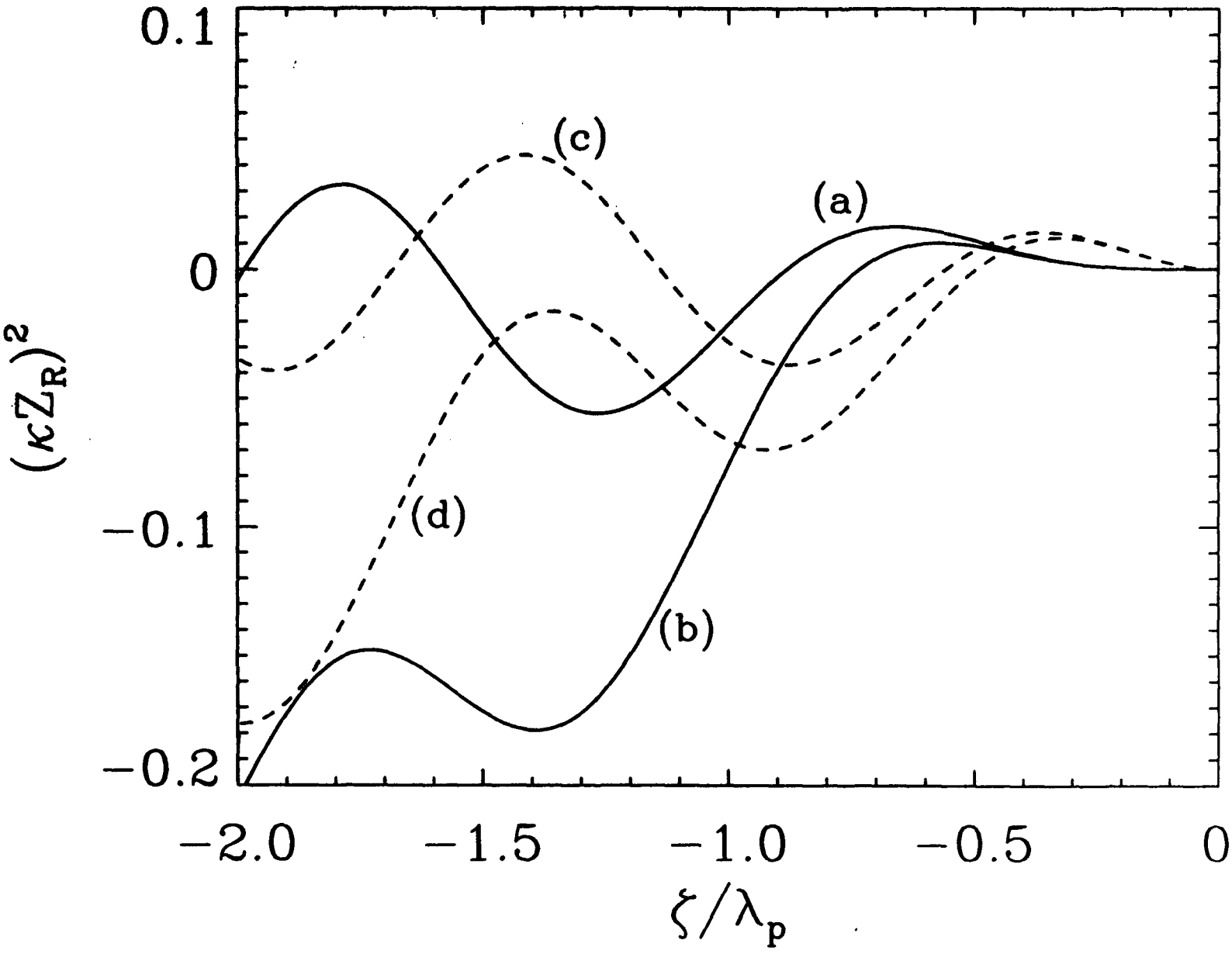


**Fig. 1 Plots of $(\kappa Z_R)^2$ versus $\zeta$ for each of four radius–tailored laser pulse configurations**

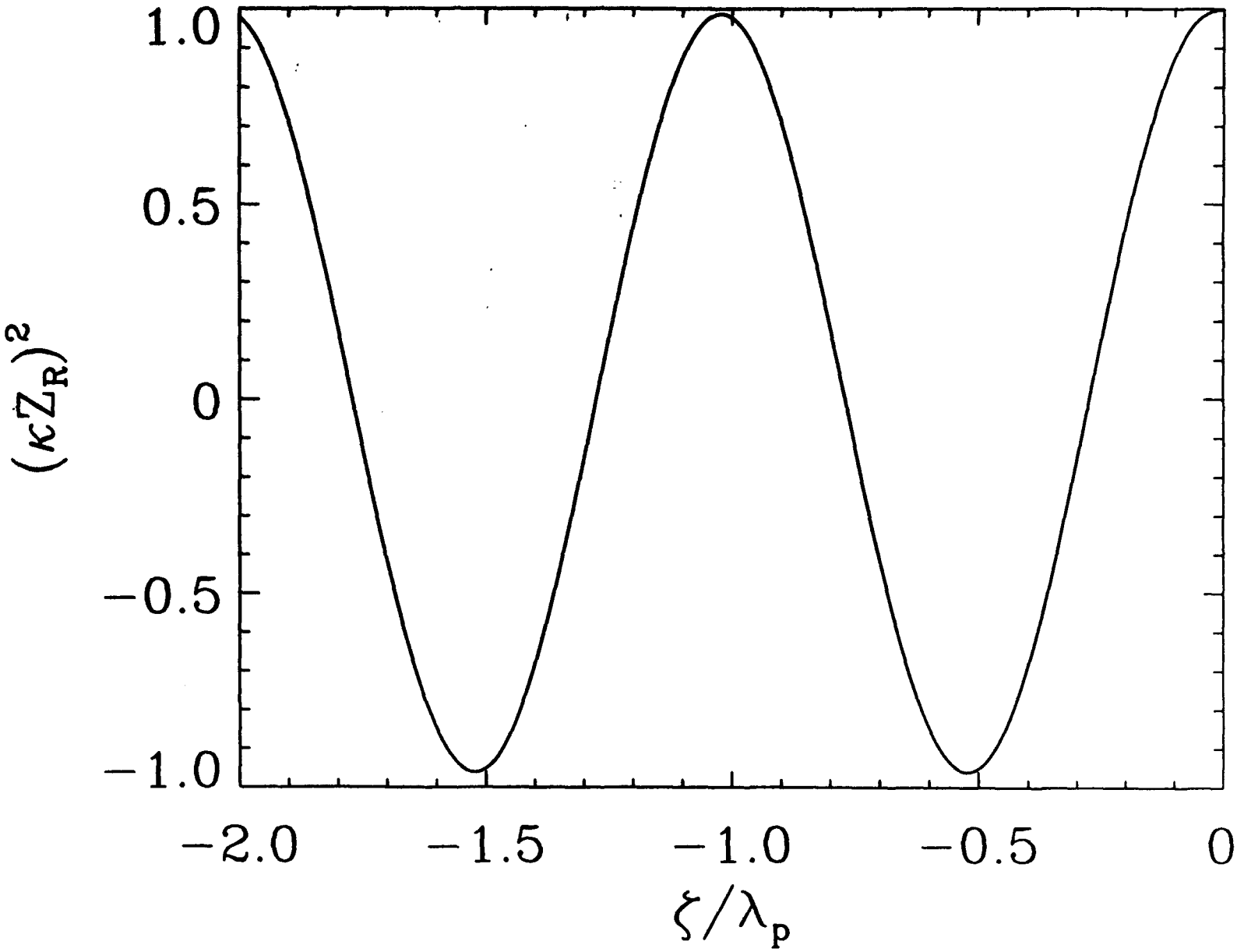


**Fig. 2 Plot showing $(\kappa Z_R)^2$ versus $\zeta$ for a rectangular pulse with $a_L = a_0, 0 \leq -\zeta \leq 2\lambda_p$, and $P = P_c$.**

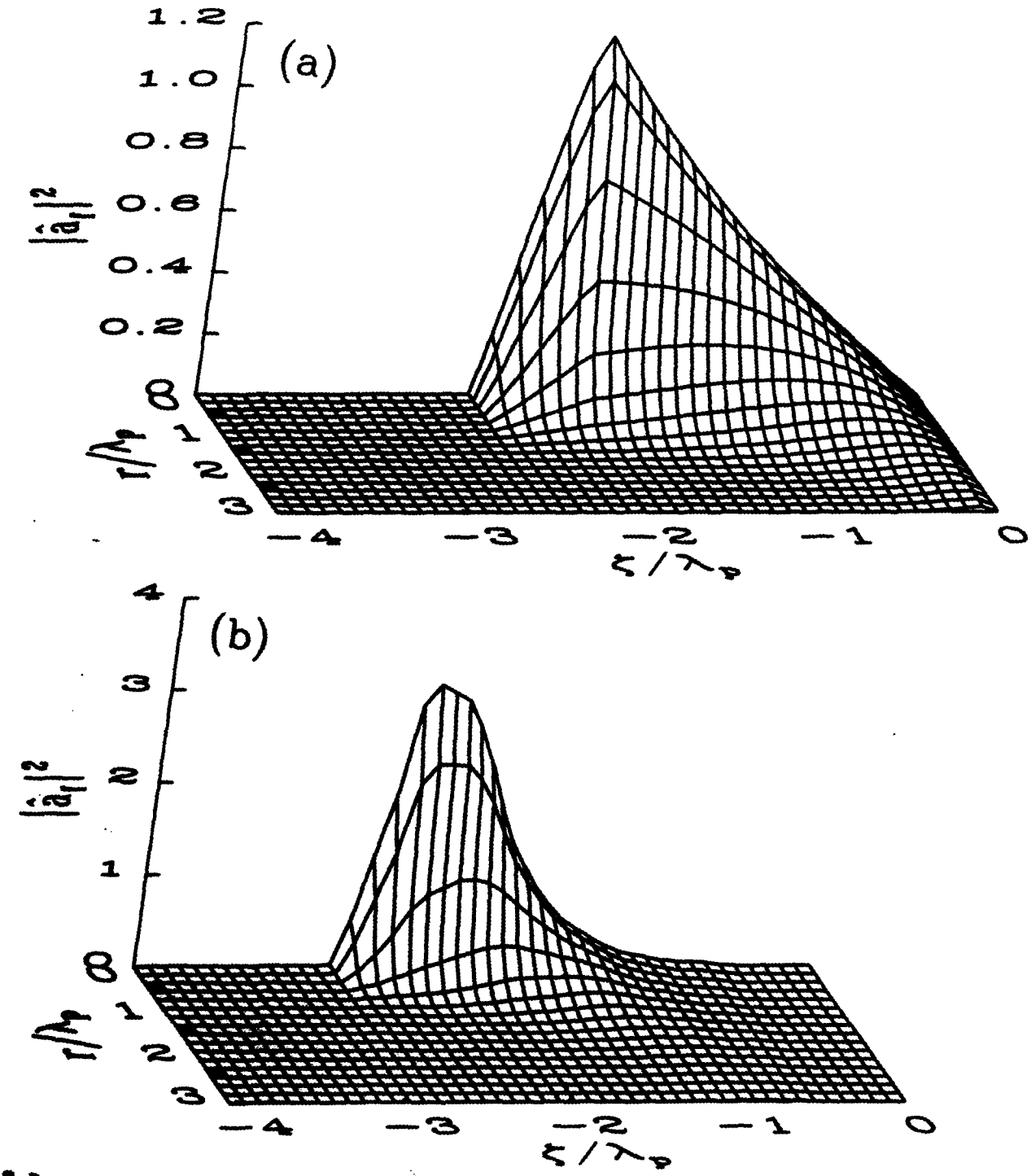


**Fig. 3** Laser intensity $|\hat{a}_f|^2$, sampled over a coarse grid (the numerical grid is much finer), at (a) $c\tau = Z_R$ and (b) $c\tau = 16Z_R$, for a radius–tailored laser pulse. The pulse is moving towards the right.

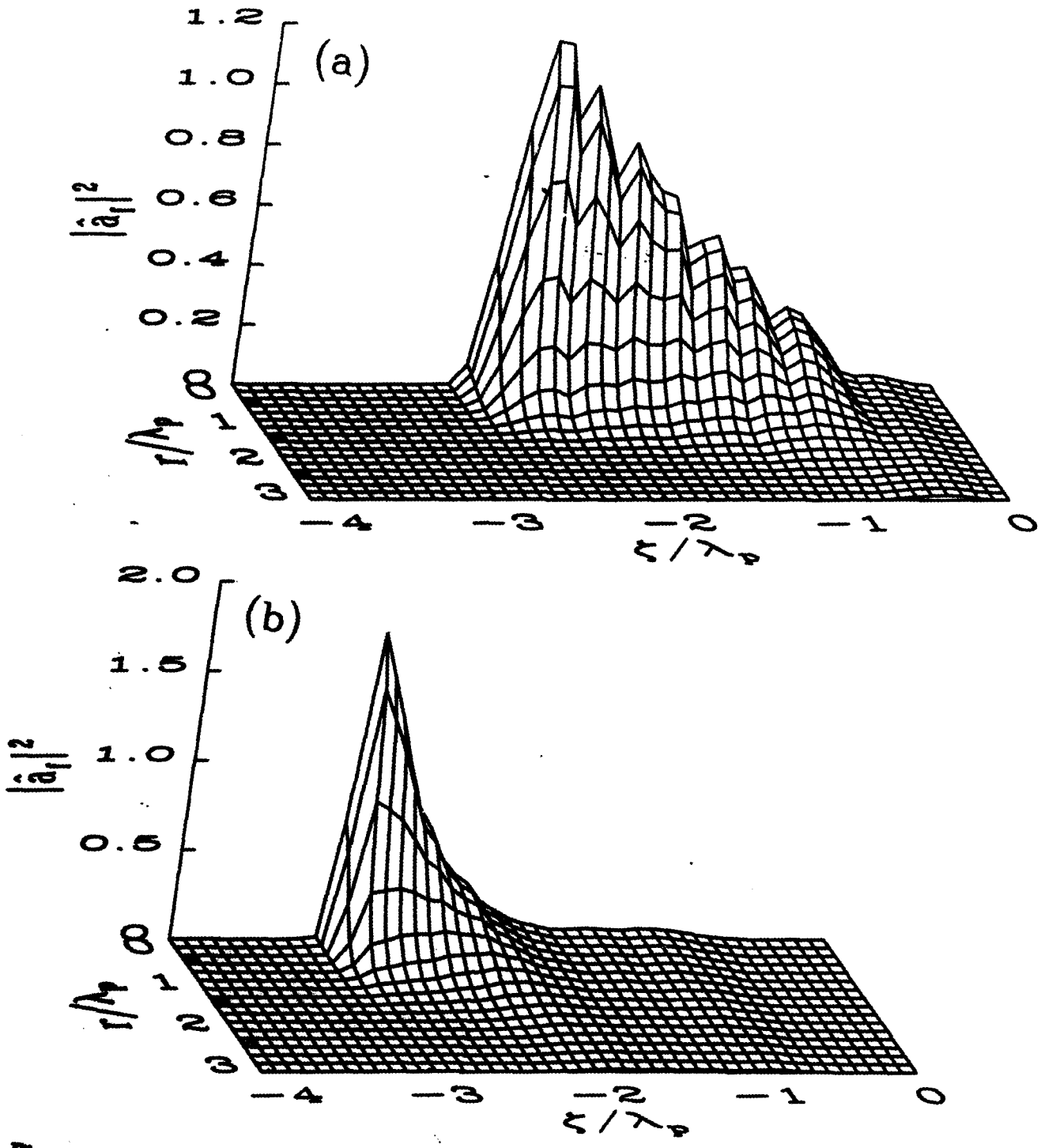


**Fig. 4** Laser intensity $|\hat{a}_1|^2$, at (a) $c\tau \approx Z_R$ and (b) $c\tau = 16Z_R$, for a radius–tailored laser pulse constructed from five phase-locked Gaussian pulses.

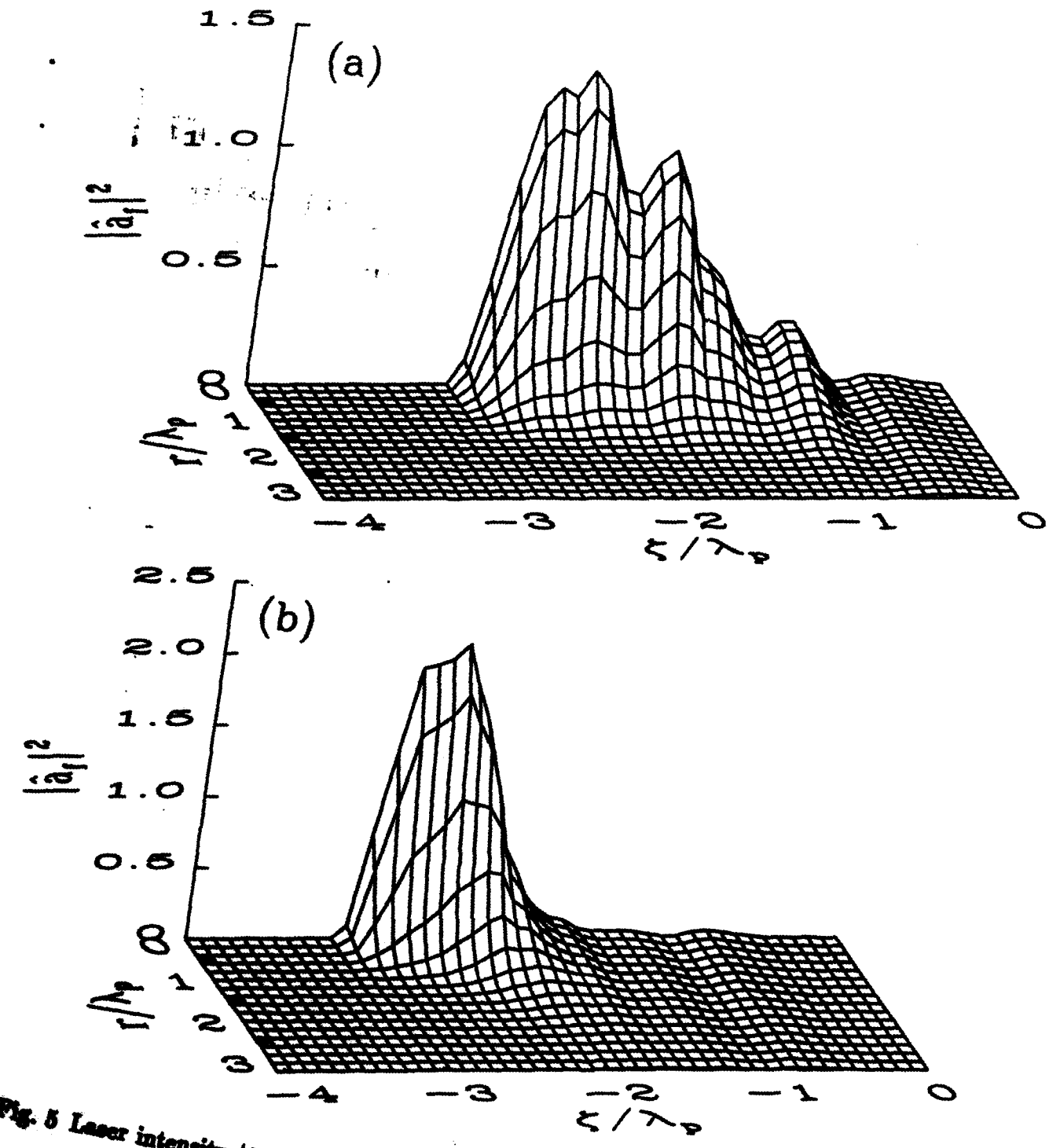


**Fig. 5** Laser intensity $|\hat{a}_f|^2$, at (a) $c\tau = Z_R$ and (b) $c\tau = 11Z_R$, for a radius–tailored laser pulse constructed from five randomly-phased Gaussian pulses.

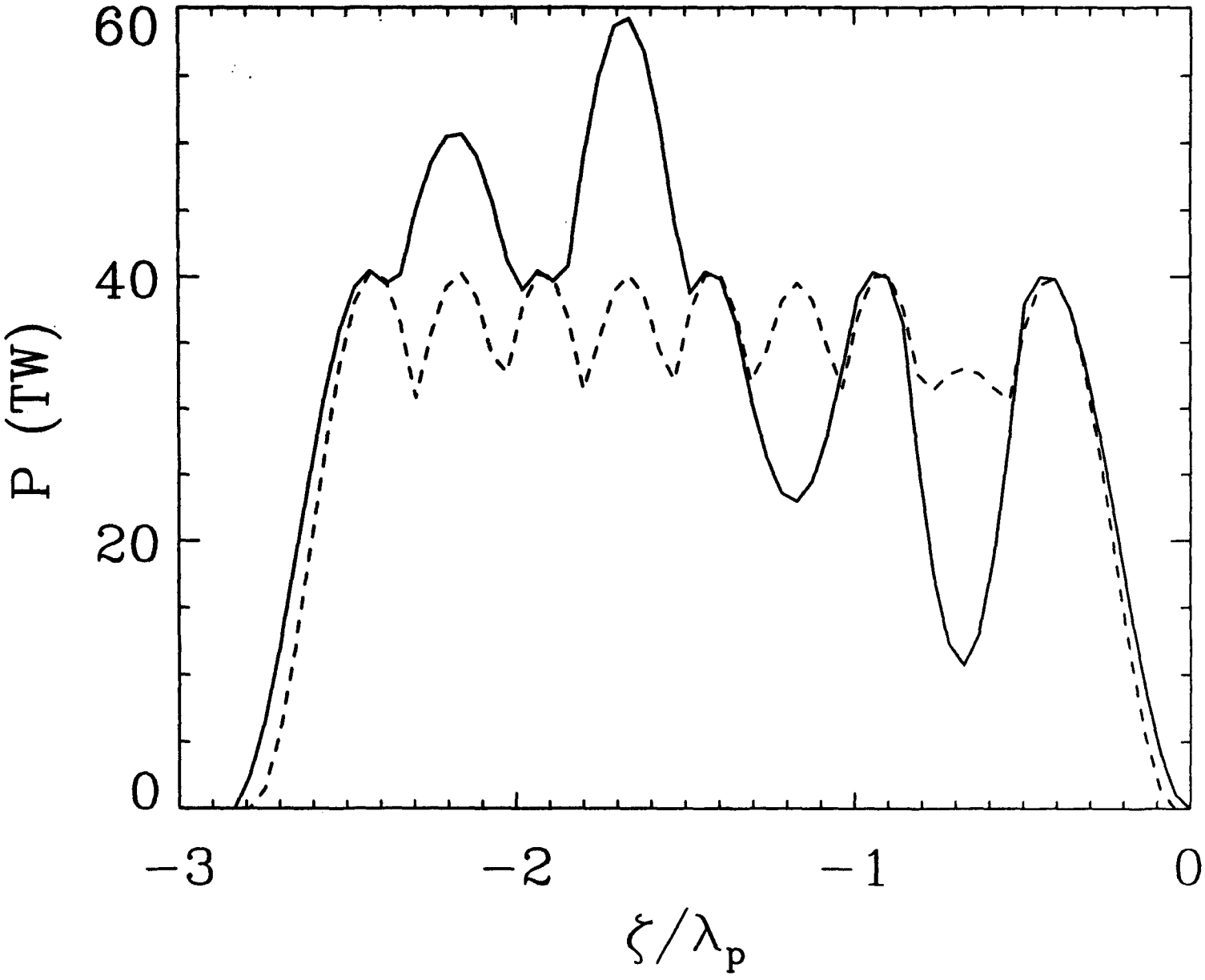


Fig. 6 Laser power $P$ versus $\zeta$ at $\tau = 0$ for the laser pulses of Fig. 5 (solid line) and Fig.